Multi-objective optimization of microchannel heat sink with Cantor fractal structure based on Pareto genetic algorithm

Helin Wang*, Xueye Chen**,†, Jianqing Hu***, and Xiangwei Zeng**

*Faculty of Mechanical Engineering and Automation, Liaoning University of Technology, Jinzhou, Liaoning 121001, China
**College of Transportation, Ludong University, Yantai, Shandong 264025, China
***Northern Heavy Industries Group Co, Ltd, Shen Yang, Liaoning, 110141, China

Abstract−Microchannel heat sinks have been widely used in high-density packaged electronic device cooling technology. We combined the cantor fractal structure with the microchannel heat sink to design a new type of microchannel structure. Combining fractal structure with microchannel heat sink is one of the cutting-edge technologies of heat transfer to solve the heat dissipation problem of high heat flux electronic equipment. We chose the width-to-height ratio of the microchannel inlet (a/b), the width-to-height ratio of the Cantor fractal baffle (B/h) and the ratio of the microchannel inlet width and the distance between each group of baffles (a/λ) as design variables, and the optimization objective was to make the global thermal resistance and pump work minimum. First, the pressure drops, temperature, and velocity of the microchannel heat sink were analyzed. Then, to consider the fluid heat transfer and pressure drop comprehensively, the enhanced heat transfer factor PEC was used to evaluate the comprehensive heat transfer performance of the microchannel. The final optimized structure PEC values were all greater than 1. In the Reynolds number (Re) range of 100-500, its enhanced heat transfer factor PEC is 1.56-1.79, which indicates that the heat transfer effect of the optimized microchannel heat sink is greatly enhanced than that of the conventional microchannel.

Keywords: Cantor Fractal, Multi-objective Optimization, Pareto Genetic Algorithm, Microchannel Heat Sink

INTRODUCTION

With the rapid development of science and technology in the 20th century, microelectromechanical systems (MEMS) are an emerging technology field, resulting in unprecedented challenges in the field of heat transfer, and micro-scale heat transfer technology has rapidly become a hot topic [1-7]. As MEMS technology advances day by day, the study of heat dissipation in electronic devices has become an important direction in the development of science and technology. The problem of electronic device failure due to high temperature has received considerable attention from scientists and scholars. This makes it urgent to develop highly efficient and low resistance microchannel heat sinks for electronic devices to maintain their reliability and lifetime, which are of great significance in cooling electronic devices with high heat flow density [8-15]. Microchannel heat exchangers have superior performance, such as compact structure, large specific surface area, high efficiency, light mass, safe. There are many factors affecting the performance of microchannel heat sinks, such as the structural dimensions of microchannels [16-25], microchannels with ribs or baffles [26-30], and fluid-solid materials [31,32]. Microchannel heat sinks are widely used in medical, aviation, chemical, refrigeration technology and many other fields [33-37].

To simulate the heat transfer performance of a silicon-based parallel microchannel heat sink, a complete three-dimensional conjugate heat transfer model was developed by Li et al. and geometric structure was optimized. The thermal resistance of the optimized microchannel heat sink was calculated based on the 3D conjugate heat transfer model for different pump power at a water-cooled heat sink power of 0.05 W and compared with the preliminary experimental results of Tuckerman and Pease in 1981. This comparison showed that the cooling capacity could be increased by more than 20% using the optimized microchannels [38].

Chen characterized the morphology of rough surfaces with Cantor set structure, based on which a rough microchannel laminar heat transfer model was developed and numerically analyzed. The effects of Re, relative roughness and fractal dimension on laminar heat transfer were investigated. The results show that the local Nusselt number after the inlet region is no longer constant but fluctuates along the rough microchannel. Unlike for smooth microchannels, the average Nusselt number increases approximately linearly with the Re, which is larger than the classical value. At higher relative roughness, flow through the roughness causes flow separation, which contributes to laminar convective heat transfer. In addition, laminar heat transfer in microchannels is also enhanced by roughness with a larger fractal dimension, which produces more frequent changes in the surface profile even at the same relative roughness [39].

Mohd used a multi-objective genetic algorithm (MOGA) to optimize the hydraulic diameter and wall width ratio of square and circular microchannels to minimize the two objective functions. The thermophysical performance of the system was obtained by measuring the average experimental saturation temperature on a horizontal microchannel test bench using liquid ammonia as the coolant.

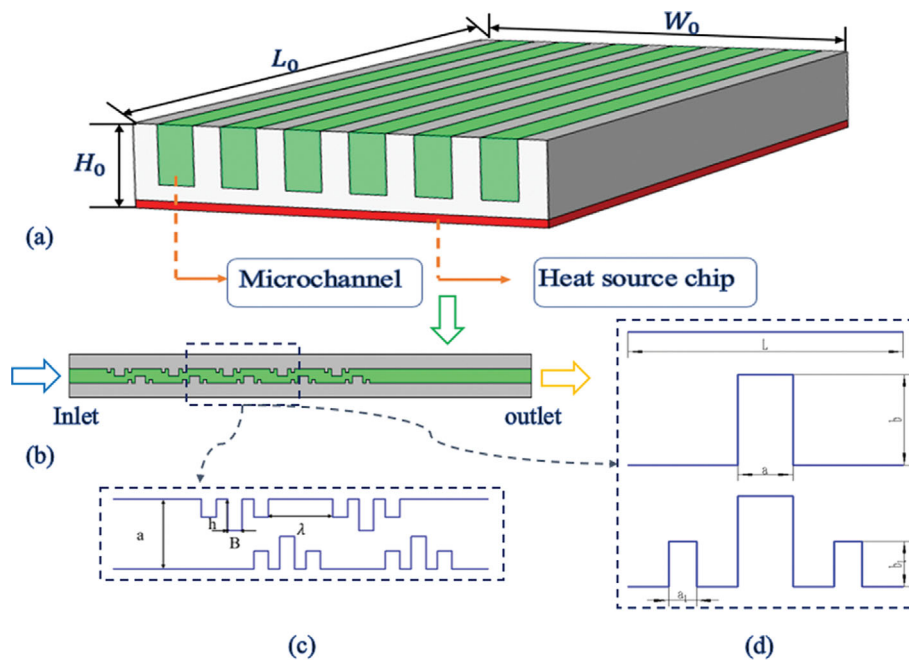†To whom correspondence should be addressed.
E-mail: xueye_chen@126.com

Fig. 1. (a) Rectangular microchannel heat sink model (b) Single microchannel model (c) Microchannel structure (d) Cantor fractal schematic.

The optimization results showed that the circular microchannel had a lower thermal resistance for the same hydraulic diameter and power [40].

Entropy generation minimization (EGM) was considered as a single objective function by Adham. Genetic algorithms (GA) were used to perform the minimization and showed extraordinary performance. In this paper, the overall performance of a rectangular microchannel heat sink under laminar and turbulent flow conditions is investigated using an effective combination of EGM and GA. The entropy yields reach their optimum values after 12, 8 and 13 generations when the volume flow rates are 0.005, 0.007 and 0.009 m^3/s, respectively. In addition, the total thermal resistance in the turbulent flow region is significantly reduced. Finally, a parametric study was carried out to investigate the effects of flow channel aspect ratio, fin spacing ratio, Re and different materials on the overall performance of the system, and good results were obtained [41].

In this paper, the pump power and thermal resistance objective functions of each design point in the design variable space are obtained, and then the surrogate model of the objective function about the optimization variables is established; the optimal solution set in the design space is obtained through the multi-objective optimization algorithm. The optimal solution is chosen according to specific needs. And the enhanced heat transfer factor PEC is used to evaluate the integrated heat transfer performance of the microchannels. It is found that combining multi-objective genetic algorithm and fractal theory can greatly improve the integrated heat transfer performance of microchannel heat sink through research and analysis.

MODELING AND THEORETICAL BACKGROUND

1. Microchannel Heat Sink Modeling

In this paper, a Cantor fractal baffles structure is set in the side

wall of a rectangular microchannel; the studied single-layer parallel rectangular microchannel heat sink is shown in Fig. 1(a). The flowing medium is deionized water, the heat sink matrix material is silicon, and the bottom of the solid is equipped with a constant heat flow density q=1.0×10^6 W/m^2. The model uses fluid-solid coupling, and the structural parameters of the solid domain are height H_0 is 0.2 mm, width W_0 is 4 mm, and length L_0 is 4 mm.

We chose to study the flow characteristics of rectangular microchannels by adding rectangular slots on the sidewalls of rectangular microchannels because the heat transfer performance of rectangular microchannels is found to be better. As shown in Fig. 1(b), Since each microchannel is arranged linearly, a single microchannel is selected for the analysis. The rectangular slots are arranged sequentially in the flow direction of the microchannels, and the sides are staggered. The overall modeling was performed using *SolidWorks 2018* software.

2. Fractal Principle

Cantor fractal principle was first introduced by the German mathematician, Georg Cantor [42]. It is the set of point sets obtained from simple linear segments. Although Cantor himself defined this point set in an abstract way, the most popular construction is the Cantor triple fractal set. Fig. 1(c) and (d) show a baffle structure based on Cantor fractal principle. A line segment of length L is divided equally into three segments. The initial length of the fractal baffle is a, the height of the first level fractal baffle is b, the height of the second level fractal baffle is b_1 and the length is a_1.

3. Boundary Conditions and Control Equations

In this paper, *COMSOL Multiphysics 5.5* software was used to perform numerical simulation analysis. This software is a numerical simulation software based on the finite element method, which can solve some partial differential equations of physical simulation. We made the following assumptions before numerical simulation

of the microchannel heat sink: The flow field distribution and heat transport processes in the microchannel are steady state. Fluid is incompressible. Thermophysical properties of solids remain unchanged. Ignoring natural convective heat transfer and jurisdictional heat transfer around the microchannel, the surfaces in contact with the outside world are thermally insulated, except for the bottom, which gives a constant heat flow. Gravity and viscous dissipation of the fluid are ignored. Under these assumptions, the control and momentum equations based on the continuous medium assumption and the Navier-Stokes equations are established.

Momentum equation:

$$\rho_f\left(u\frac{\partial u}{\partial x}+u\frac{\partial v}{\partial y}+u\frac{\partial w}{\partial z}\right)=\mu\left(\frac{\partial^2 u}{\partial^2 x}+\frac{\partial^2 u}{\partial^2 y}+\frac{\partial^2 u}{\partial^2 z}\right)-\frac{\partial p}{\partial z} \tag{1}$$

$$\rho_f\left(v\frac{\partial u}{\partial x}+v\frac{\partial v}{\partial y}+v\frac{\partial w}{\partial z}\right)=\mu\left(\frac{\partial^2 u}{\partial^2 x}+\frac{\partial^2 u}{\partial^2 y}+\frac{\partial^2 u}{\partial^2 z}\right)-\frac{\partial p}{\partial y} \tag{2}$$

$$\rho_f\left(w\frac{\partial u}{\partial x}+w\frac{\partial v}{\partial y}+w\frac{\partial w}{\partial z}\right)=\mu\left(\frac{\partial^2 u}{\partial^2 x}+\frac{\partial^2 u}{\partial^2 y}+\frac{\partial^2 u}{\partial^2 z}\right)-\frac{\partial p}{\partial z} \tag{3}$$

where, u, v, w is the partial velocity in the x, y, z direction, m/s; μ: the dynamic viscosity of the fluid, Pa·s; ρ_f the density of the internal fluid workpiece, kg/m^3.

Continuity equation:

$$\frac{\partial u}{\partial x}+\frac{\partial v}{\partial y}+\frac{\partial w}{\partial z}=0 \tag{4}$$

Energy equation:

$$\rho_f\cdot c_V\left(u\frac{\partial T}{\partial x}+u\frac{\partial T}{\partial y}+u\frac{\partial T}{\partial z}\right)=\lambda_f\left(\frac{\partial^2 T}{\partial^2 x}+\frac{\partial^2 T}{\partial^2 y}+\frac{\partial^2 T}{\partial^2 z}\right) \tag{5}$$

where, T is the thermodynamic temperature, K; c_V is the specific heat capacity of the fluid, J/(Kg·K); λ_f is the thermal conductivity of water, W/m·K.

The initial conditions set are: The working fluid inlet temperature of the rectangular baffles microchannel heat sink is 300 K and the initial velocity is v. The inlet of the rectangular baffles microchannel is set as velocity inlet and the outlet is set as pressure as outlet. The contact surface between the working fluid and the wall of the microchannel heat sink is set as a no-slip boundary condition. The intersection of the working fluid and the solid wall is set to the fluid-solid coupling boundary. Constant heat flow rate is applied by the heat source chip to the rectangular baffles microchannel heat sink substrate.

The hydraulic diameter is the ratio of four times the cross-sectional area of the fluid to the wet perimeter, defined by the equation:

$$D_h=\frac{4A_c}{P} \tag{6}$$

where, A_c is the channel inlet cross-sectional area, P is the wet perimeter. In this paper the design of the inlet is rectangular, the height is H, the width is W, and the hydraulic diameter is calculated by the formula:

$$D_h=\frac{2HW}{H+W} \tag{7}$$

Newton's cooling equation, as the basic equation for convective heat transfer, is defined as follows:

When the fluid is heated:

$$q=\overline{h}(t_w-t_f) \tag{8}$$

When the fluid is cooled:

$$q=\overline{h}(t_f-t_w) \tag{9}$$

where $\overline{h}$: convective heat transfer coefficient (also known as surface heat transfer coefficient), W/(m^2·K), t_w and t_f are the average solid wall temperature and the average fluid temperature, respectively. In this paper, the numerical simulation is carried out under the condition of constant heat flow density at the bottom. Then the convective heat transfer coefficient is:

$$\overline{h}=\frac{q}{(t_w-t_f)} \tag{10}$$

The physical meaning of Re is the ratio of the inertial force to the viscous force and is a dimensionless number used to characterize fluid flow. Re is defined as:

$$Re=\frac{\rho v D_h}{\mu} \tag{11}$$

where, ρ: fluid density, kg/m^3; v: average inlet flow velocity, m/s; D_h: hydraulic diameter mm; μ dynamic viscosity, Pa·s.

The Fanning friction factor f [43], named after John Thomas Fanning, is a dimensionless number used as a local parameter in continuous medium calculations. It is defined as the ratio of local shear stress to local flow kinetic energy density.

$$f=\frac{D_h}{L}\frac{2\Delta P}{\rho u^2} \tag{12}$$

where, ΔP: inlet and outlet pressure drop, Pa; L: length of microchannel, mm.

The Nusselt number is a dimensionless number that represents the strength of convective heat transfer, the physical meaning is the ratio of the thermal resistance of the bottom layer of the fluid laminar flow to the convective heat transfer thermal resistance. The formula is defined as follows:

$$Nu=\frac{\overline{h}D_h}{\lambda} \tag{13}$$

where, λ: thermal conductivity, W/(m·K), D_h: hydraulic diameter, mm; h: heat transfer coefficient, W/(m^2·K).

The Prandtl number is a dimensionless parameter characterizing the relative importance of momentum exchange and heat exchange in fluid flow and it reflects the effect of the physical properties of the fluid on the convective heat exchange process.

$$Pr=\frac{C_P\mu}{\lambda} \tag{14}$$

where C_P is the specific heat capacity of the fluid at constant pressure, J/(kg·K).

Colburn in the study of heat and mass transfer proposed the heat transfer factor j [43], which is a dimensionless number describing

the strength of heat transfer. It is defined as:

$$J = \frac{h Pr^{2/3}}{\rho C_p u} \tag{15}$$

To integrate the heat transfer and pressure drop of the fluid, it is pointed out that the enhanced heat transfer factor PEC [44] is more reasonable than the entropy yield and heat transfer coefficient to evaluate the integrated heat transfer performance of the microchannel. The enhanced heat transfer factor is based on the relationship between the power consumption of the pump (fan) proportional to the third power of the rotational speed, and the evaluation method derived under the condition of equal power consumption.

The enhanced heat transfer factor is expressed as follows

$$PEC = \left(\frac{Nu}{Nu_0}\right) \Big/ \left(\frac{f}{f_0}\right)^{1/3} \tag{16}$$

where the relevant physical quantities of the conventional microchannel carry the subscript 0.

4. Verification of Mesh Independence

To verify the accuracy of the calculation, we verified the mesh independence. As shown in Fig. 2(a), we tested four meshes, 157,524, 384,181, 702,889 and 1,988,540, when the flow velocity was 0.7856 m/s. We studied the velocity distribution at the exit (Z=0-0.1 mm) under four different meshes. The greater the number of meshes, the more accurate the simulation results, but the more time the simulation process takes. Therefore, while satisfying accuracy, we save calculation time as much as possible. We chose mesh 3 for the numerical simulation of this article. In Fig. 2(b), we quote the re-

search results of Yang Liu et al. and compare the numerical results of this paper [45]. Since the model in this article is unique, we quote the most similar model for data comparison. It can be seen from the figure that the two results can be matched well, and the error is within an acceptable range. It can be seen that as the flow rate increases, the outlet temperature of the microchannel in this study is lower, which improves the heat transfer effect of the microchannel.

MULTI-OBJECTIVE OPTIMIZATION

1. Design Variables and Objective Functions

Choosing the appropriate design variables to influence the heat transfer performance is important for design optimization. As shown in Fig. 3, we chose the width-to-height ratio of the microchannel inlet (a/b), the width-to-height ratio of the Cantor fractal baffle (B/h) and the ratio of the microchannel inlet width and the distance between each set of baffles (a/λ) as design variables. Based on experimental studies and constraints of the model, the design variables are set within a reasonable range, the width of the microchannel a=0.1 mm, and the width of the cantor fractal baffle structure B= 0.09 mm. Since the height of the microchannel is 0.2 mm, so the design range of b is 0.1-0.18 mm. The baffle structures on both sides of the microchannel are symmetrically distributed, so the design range of h is 0.03-0.05 mm. The overall length of the microchannel is 4 mm, and the number of baffle structures varies. Therefore, the design range of h is 0.2-0.4 mm. Table 1 shows these design variables and their ranges.
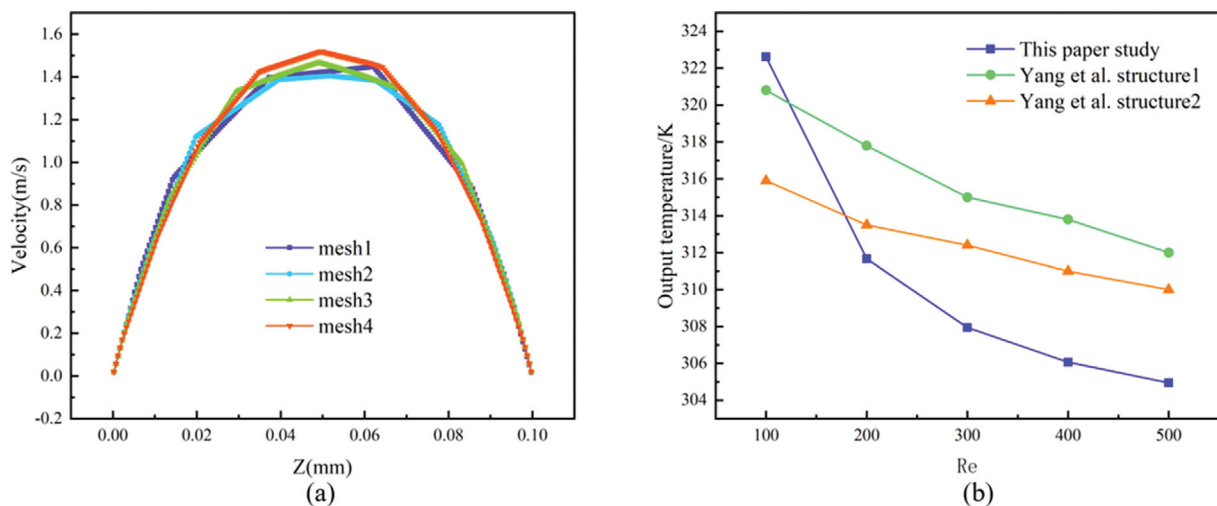

Fig. 2. (a) Verification of mesh independence (b) Comparison of the study in this article with other studies.
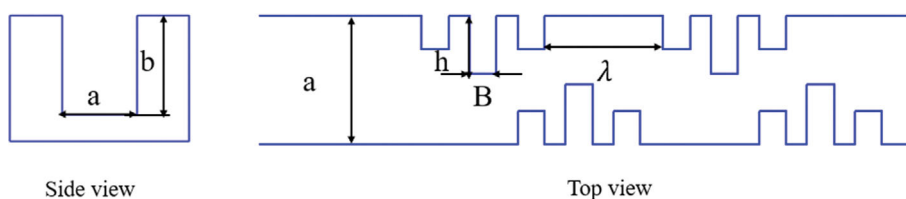

Fig. 3. Design variables of Cantor fractal structure in microchannel radiator.

Table 1. The value range of the design variables

Range	Design variables		
	a/b	B/h	a/λ
Minimum (min)	0.56	1.8	0.25
Maximum (max)	1	3	0.5

The optimization objective is to minimize the global thermal resistance R_t and the pump work P_p for a certain volume flow rate of the microchannel heat sink working medium by selecting different sets of three design variables [40]. The global thermal resistance is defined as:

$$R_t = \frac{T_{s,max} - T_{f,in}}{qA_s} \tag{17}$$

where: A_s is the area of the bottom of the microchannel heat sink; $T_{s,max}$ is the maximum temperature of the heat sink; $T_{f,in}$ is the fluid medium inlet temperature. Pump work is defined as.

$$P_p = NuA_c\Delta p \tag{18}$$

where: Δp is the pressure drop across the microchannel; u is the average flow rate of the medium in the microchannel; A_c is the cross-sectional area of a single microchannel; and N is the number of micropasses. We have chosen the global thermal resistance R_t and the pump work P_p as the objective functions, and the present multi-objective optimization problem can be described as [41]:

$$\text{V-min} \quad F(x) = [f_1(x), f_2(x), ..., f_n(x)]^T \tag{19}$$
$$\text{Min} \leq x \leq \text{Max}, \quad x \in R$$

where V-min is the minimization of the vector, namely, each sub-objective function in the vector target $f_i(x)$ is minimized as much as possible, F(x) is the vector of the objective function, and x is the vector of the design variable. Min and Max are, respectively, the boundary value of the range of the design variable range.

We take the global thermal resistance R_t and the pump work P_p of the microchannel heat sink as objective functions. Since the multi-objective optimization is to find the minimum value, $f_1(x)=R_t$, $f_2(x)=P_p$.

We constructed the design space using design of experiments (DOE) and determined the design points within the design range using the Latin hypercube sampling (LHS) method. To obtain the LHS design points, we used the 'lhsnorm' function on *Matlab R2018a* to select 30 uniformly distributed points for the three design variables. *COMSOL Multiphysics 5.5* software was used to perform the numerical simulation analysis. This software is a numerical simulation software based on the finite element method, which can solve some partial differential equations of physical simulation. The software is used to simulate the design points and calculate the objective function values. Table 2 lists the objective function values calculated by Navier-Stokes analysis for these design points for Re=100. In this sampling scheme, the homogeneity of the sampling scheme is maintained by measuring the maximum and minimum distances between the design points.

The response surface analysis (RSA) method was used to establish the agent model of the above design points. Then, a multi-objec-

Table 2. Design variables and objective function values at Re=100

Design points	Design variables			Objective functions	
	a/b	B/h	a/λ	P_p (Re=100)	R_t (Re=100)
1	0.5711	2.8571	0.2756	0.1899	29.5667
2	0.7968	2.8939	0.2623	0.2119	34.8917
3	0.6640	2.2113	0.4437	0.3110	32.1417
4	0.5886	1.9737	02613	0.4029	28.3083
5	0.7267	1.8480	0.3063	0.5497	32.1583
6	0.6050	2.7607	0.4556	0.2150	31.1417
7	0.6464	2.1739	0.3911	0.2921	31.4333
8	0.8780	2.2843	0.3232	0.3102	35.7750
9	0.8703	2.9801	0.2554	0.2070	36.2917
10	0.7949	2.4523	0.2545	0.2580	33.6250
11	0.5744	2.7108	0.4320	0.2050	30.1333
12	0.7974	1.9608	0.2537	0.4686	32.6500
13	0.6196	2.4862	0.2555	0.2362	29.9833
14	0.8039	2.2167	0.3366	0.3289	34.7083
15	0.5784	2.7027	0.2777	0.1935	29.3333
16	0.7407	2.1429	0.4378	0.3390	33.7500
17	0.8354	2.5496	0.3516	0.2579	35.6917
18	0.7994	2.0882	0.2610	0.3669	33.1083
19	0.6188	2.0548	0.2790	0.3605	29.5917
20	0.6789	2.0000	0.2552	0.3736	30.1750
21	0.7396	2.3077	0.3020	0.2839	33.0583
22	0.6988	2.8391	0.4829	0.2032	33.6833
23	0.6309	2.6011	0.2704	0.2162	30.5167
24	0.6452	1.8634	0.2585	0.4936	29.3750
25	0.6592	2.7273	0.2979	0.2119	31.8417
26	0.7776	1.9355	0.2845	0.4575	32.8000
27	0.5692	2.2059	0.2869	0.2920	28.6500
28	0.5701	1.8036	0.3592	0.5337	28.7917
29	0.7246	2.8481	0.3020	0.1978	33.6000
30	0.6378	2.3136	0.4270	0.2687	31.3250

Table 3. Reference design and its objective functions values

Reference design					
Design variables			Objective functions		
a/b	B/h	a/λ	P (Re=100)	R (Re=100)	
0.9653	2.8939	0.2519	0.2313	37.79	

tive genetic algorithm was used to optimize the design variables in the design range to obtain the Pareto optimal frontier solution set. The objective function values of the reference design are listed in Table 3.

2. Proxy Modeling

The mathematical method of RSA is used to model the agent of the objective function [41], whose general expression is:

$$y(x) = \beta_0 + \Sigma_{i=1}^N \beta_i X_i + \Sigma_{i=1}^N \beta_{ii} X_i^2 + \Sigma_{i<j}^N \beta_{ij} X_i X_j \tag{20}$$

where x is the design variable and N is the number of design variables. In this paper, N=3; for the second-order polynomial model

Table 4. Proxy modeling plausibility check

Proxy modeling	R^2	R^2_{adj}
Thermal resistance	0.9981	0.9972
Pump power	0.9810	0.9725

Table 5. Optimal set of solutions

Design variables		
a/b	B/h	a/λ
0.5622	2.9659	0.4987
0.5647	2.0875	0.4991
0.5716	1.9332	0.4995
0.5630	1.9836	0.4997
0.5600	1.8000	0.5000

used in this paper, β is the coefficient.

For the design variables and objective functions in Table 2, the MATLAB multivariate nonlinear fitting tool was used to obtain the proxy model expressions as:

$$R_t = 2.615688395 + 0.540268512*x(1) - 2.010873895*x(2)$$
$$+ 0.746223573*x(3) - 0.193674993*x(1)^2 - 0.147164649*x(2)^2$$
$$+ 0.123766116*x(3)^2 + 0.059825221*x(1)*x(2)$$
$$+ 0.384435511*x(1)*x(3) - 1.296339446*x(2)*x(3) \quad (21)$$

$$P_p = -0.106119445 + 40.4236024*x(1) + 0.308465796*x(2)$$
$$+ 39.25272431*x(3) + 1.816254095*x(1)^2 + 11.03135924*x(2)^2$$
$$- 4.065281508*x(3)^2 - 18.13794826*x(1)*x(2)$$
$$+ 0.294723937*x(1)*x(3) - 41.30556754*x(2)*x(3) \quad (22)$$

Calculating the coefficient of determination R^2 and adjusting the coefficient of determination R^2_{adj} belong to the analysis of variance method to test the credibility of the proxy model, which is used to measure the degree of agreement between the fitted formula and the actual value, and the closer R^2 and R^2_{adj} are to 1 the better the fit is, and R^2 and R^2_{adj} are defined as [46]:

$$R^2 = \frac{\Sigma_{i=1}^{Z}(\hat{y}_i - \bar{y}_i)^2}{\Sigma_{i=1}^{Z}(y_i - \bar{y}_i)^2} \quad (23)$$

$$R^2_{adj} = 1 - \frac{(Z-1)\Sigma_{i=1}^{Z}(\hat{y}_i - y_i)^2}{(Z-1-g)\Sigma_{i=1}^{Z}(y_i - \bar{y}_i)^2} \quad (24)$$

where Z is the number of experimental points; in this paper Z= 30; g is the degree of freedom of design variables, equal to the number of design variables minus 1; y_i, $\hat{y}_i$, $\bar{y}_i$ are the true values at the experimental points, the predicted values of the fitted curve and the average of the true values at the experimental points, respectively. The results of R^2 and R^2_{adj} of this fit are shown in Table 4, and their values are greater than 0.97, indicating that the fitted results are in good agreement with the experimental point results, and the confidence of the fit is high, which can be used for the next optimization analysis.

3. Multi-objective Genetic Optimization

The sub-objectives in a multi-objective optimization problem are generally opposed to each other, and a change in one sub-objective may cause another or several other sub-objectives to become worse. In this paper, for example, as the height-to-width ratio (a/b) of the microchannel inlet increases, the pressure drop increases and the thermal resistance decreases; as the width-to-height ratio (B/h) of the Cantor fractal baffle increases, the pressure drop decreases and the thermal resistance increases; as the ratio of the width of the microchannel inlet and the distance between each group of baffles (a/λ) increases, the pressure drop increases and the thermal resistance decreases. Therefore, each sub-objective can only be coordinated and traded off according to the priority and weight of different sub-objectives, so that each sub-objective can be optimized

as much as possible. As shown in Table 5, the essential difference between multi-objective optimization and single-objective optimization problem is that its solution is not unique, but there is a set of optimal solutions consisting of many Pareto optimal solutions, and each element in the set is called Pareto optimal solution or non-inferior optimal solution:

RESULTS AND DISCUSSION

Based on the optimal solutions obtained by the multi-objective genetic algorithm, we selected a set of b=0.18 mm, h=0.05 mm, and λ=0.2 mm as the optimized final structure. The optimized fractal microchannel and its corresponding reference microchannel and regular rectangular microchannel are named as Optimized microchannel, Reference microchannel and R-Optimized microchannel, respectively.

1. Flow Characteristics Analysis

Fig. 4(b), (c), (d) show the overall and four cross-sectional pressure clouds of the microchannel. There are more red areas near the entrance of the channel, indicating that the entrance pressure is higher. The fluid pressure of the microchannel heat sink gradually decreases from the inlet to the outlet. After adding the baffle of the cantor fractal structure in the microchannel, the heat exchange area of the entire channel is increased, which leads to a sharp increase in the pressure drop in the channel.

The pressure drop in the cantor fractal microchannel is obviously greater than the pressure drop in the smooth channel, indicating that if the heat transfer performance of the microchannel is improved, an increase in pressure drop is inevitable. Therefore, we usually choose microchannels with the goal of low global thermal resistance and low pump power.

Fig. 4(a) shows the variation of pressure drop with Re for different microchannels; the pressure drop gradually increases with the increase of Re, and the setting in the baffles makes the internal heat transfer area increase, which leads to the further increase of pressure drop.

To further analyze the internal heat transfer characteristics, we analyzed velocity vector plots inside the microchannels. From Fig. 5(a), the fluid inside the optimized microchannel generates rotation and locally forms a state of vortex. The increase of fluid perturbation reduces the thickness of the boundary layer and increases the circulation area, which can strengthen the local heat transfer.

The variation relationship of friction factor with Re can be obtained from Fanning friction equation as shown in Fig. 5(b). In the range of Re 100-500, the friction factor f gradually decreases with
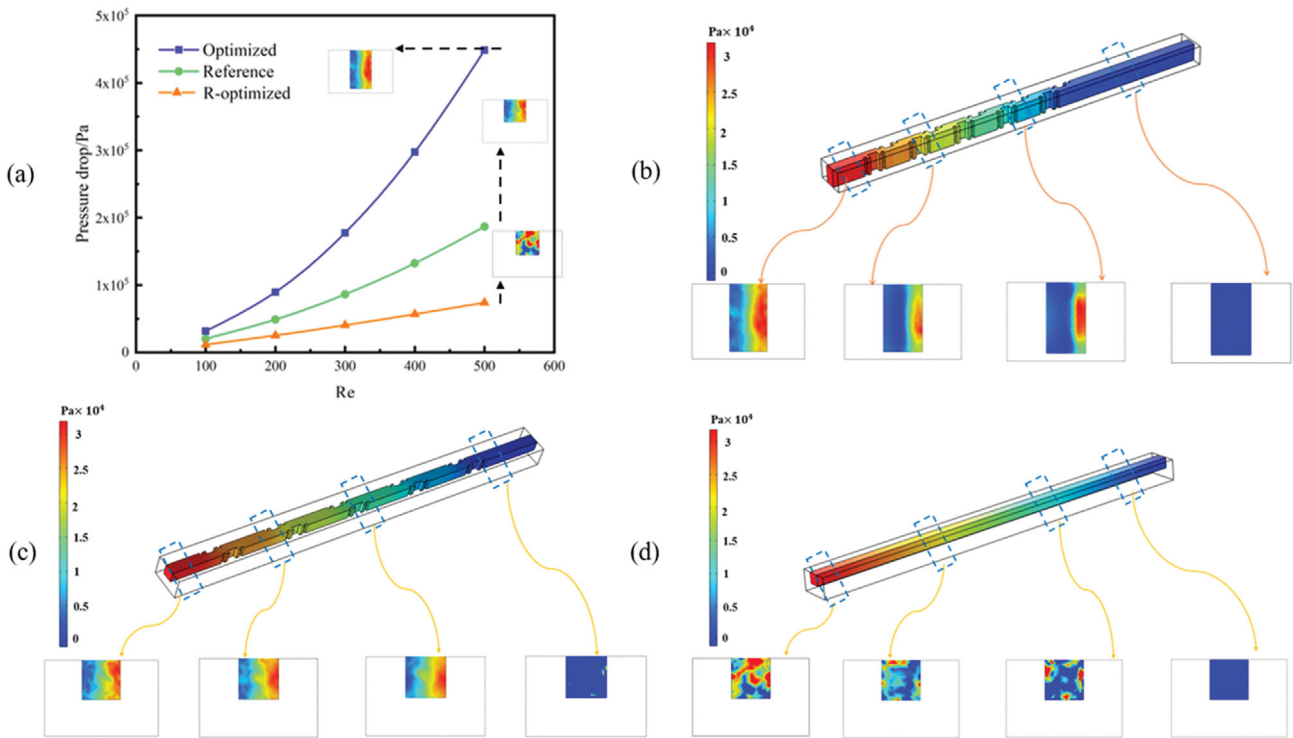
Fig. 4. (a) The variation of pressure drops at different Res (b) Optimized Pressure drop distribution (c) Reference Pressure drop distribution (d) R-optimized Pressure drop distribution.
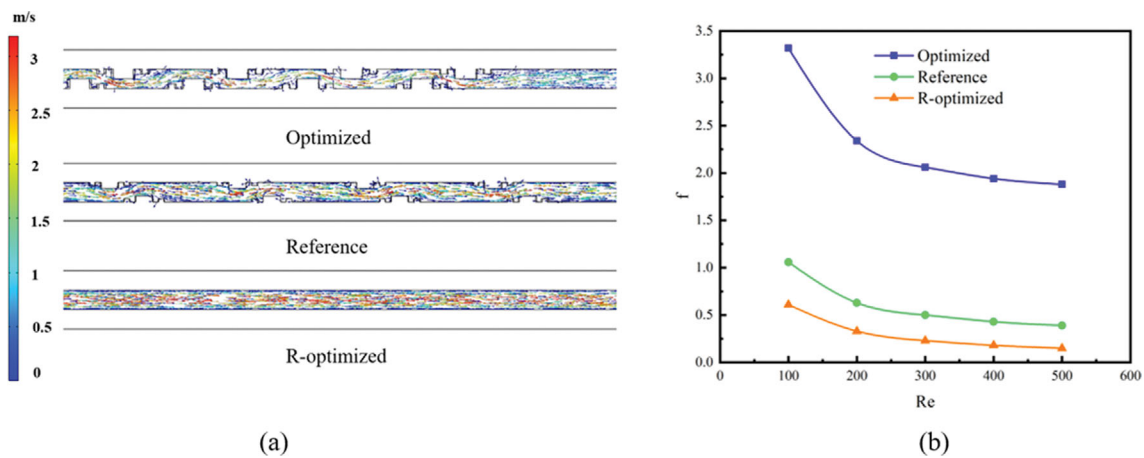

Fig. 5. (a) Velocity vectors in microchannels with different structures (b) The variation of friction factor at different Res.

the increase of Re for the microchannel heat sink. where the optimized microchannel friction factor is the largest and the smooth rectangular microchannel friction factor is the smallest. From the simulation results, the presence of the baffles structure increases the contact area, which makes the flow resistance increase and thus leads to an increase in pressure drop.

2. Comparison of Maximum Surface Temperature

In the research process of electronic chip heat dissipation, the maximum temperature that the electronic chip can withstand is limited, generally at a maximum of about 100 ^{o}C. This makes the variation of the maximum surface temperature particularly important when studying the heat exchanger used for electronic chip heat

dissipation. The maximum surface temperature variation at a heat flow density of 1.0×10^6 W/m^2, a Re of 100, and an inlet temperature of 300 K is shown in the figure, and the maximum surface temperature variation for three different structures of microchannels is shown in the following Table 6.

Table 6. Maximum microchannel surface temperature

Microchannel model	Maximum surface temperature
Optimized	321.20 K
Reference	345.35 K
R-optimized	348.20 K

Fig. 6. Maximum microchannel surface temperature.

Fig. 7. Temperature distribution at the bottom of the microchannel.
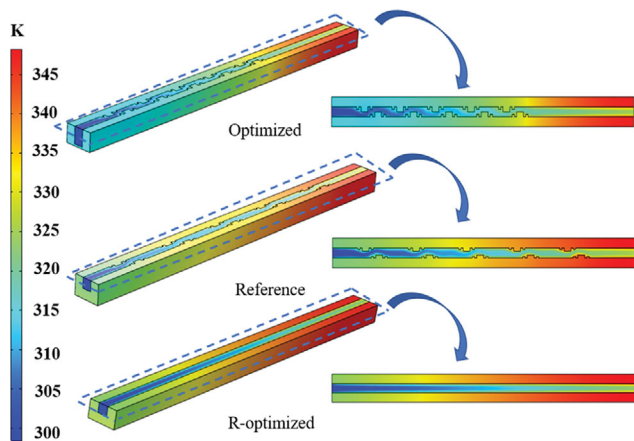
In the simulation study of three different structured microchannels, the maximum surface temperature of the optimized microchannel is 321.20 K, the maximum surface temperature of the reference microchannel is 345.35 K, and the maximum surface temperature of the conventional rectangular microchannel is 348.20 K. The optimized microchannel has the lowest maximum surface temperature, which is 24.15 k lower than the maximum surface temperature of the reference microchannel, or 6.99% lower than the maximum surface temperature of the reference microchannel, and 27 k lower than the maximum surface temperature of the conventional rectangular microchannel, or 7.75% lower. The maximum surface temperature of the optimized microchannel is lower than that of the reference microchannel by 24.15 k, or 6.99%, and by 27 k, or 7.75%, than that of the conventional rectangular microchannel. The results show that the baffles increase the internal heat transfer area, significantly reduce the maximum surface temperature of the microchannel model and optimize the heat dissipation capacity of the microchannel.

The temperature clouds of the three different structures of the microchannels are shown in Fig. 6, where the temperature of the fluid and the solid gradually increases from the inlet to the outlet. By comparison, it is obvious that there is a significant decrease in temperature at the location where the baffles are set in the fluid domain, indicating that the presence of the baffles structure strengthens the local heat transfer, while there is no more obvious local temperature change in the conventional microchannel. On the one hand, the setting of the baffles increases the heat transfer area, which increases the heat flux under the premise of a certain heat flow density and thermal conductivity; and on the other hand, the setting of the baffles increases the fluid perturbation. The change of temperature color band shows that the blue area of the optimized microchannel is significantly increased, which indicates that the setting of the baffles optimizes the heat dissipation capacity of the microchannel.

The temperature distribution at the bottom of the microchannel is an important indicator to measure the performance of the microchannel heat sink. The lower the temperature at the bottom of the microchannel, the better the performance of the microchannel heat sink. Fig. 7 shows the sub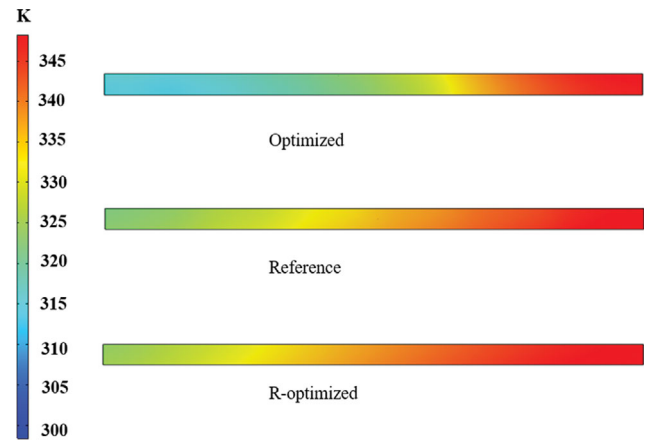strate temperature distribution under three different operating conditions. As the heat flux of constant heat flow is added at the bottom of the microchannel, the temperature at the entrance of the channel is relatively low, and with the flow of fluid the liquid in the channel continuously absorbs heat from the substrate making the temperature rise on the chip become slower; the heat absorbed at the back is less and less, and the transition from blue to red from left to right, so the temperature presented by the substrate on the chip of partial heat source becomes higher and higher. The change of temperature color band shows that the blue area of the optimized microchannel is significantly increased, which indicates that the setting of the baffles optimizes the heat dissipation capacity of the microchannel.

As shown in Fig. 8(a), Nu increases with the increase of Re for different structures, which indicates that the increase of Re can strengthen the internal heat transfer. From the images, the optimized microchannel structure is much higher than the reference microchannel and the conventional rectangular microchannel, indicating that the setting of the baffles structure strengthens the internal heat transfer in the microchannel. Due to the increase of Re, the velocity of the fluid inside the microchannel is accelerated. At the same time, the contact area is indirectly increased, so that more heat can be taken away and the effect of heat transfer can be improved. As shown in Fig. 8(b), with the increase of Re, j decreases with different structures of microchannels, and the change trend is similar, which indicates that the increase of Re can still strengthen the heat transfer between the fluid and the wall even in the laminar flow regime. The heat transfer factor is much higher than that of the conventional microchannel after setting the baffles structure. At the same Re, the conventional rectangular microchannel has the smallest j and the worst heat transfer effect, while the optimized microchannel has the largest heat transfer factor and the best heat transfer effect. Taking the Re of 100 as an example, the j of the optimized microchannel is nearly 2.5 times higher than that of the conventional rectangular microchannel. It indicates that the geometry of the microchannel has an important influence on the heat transfer of the fluid.

3. The Average Substrate Temperature and Pressure Drop after Optimization with Different Res

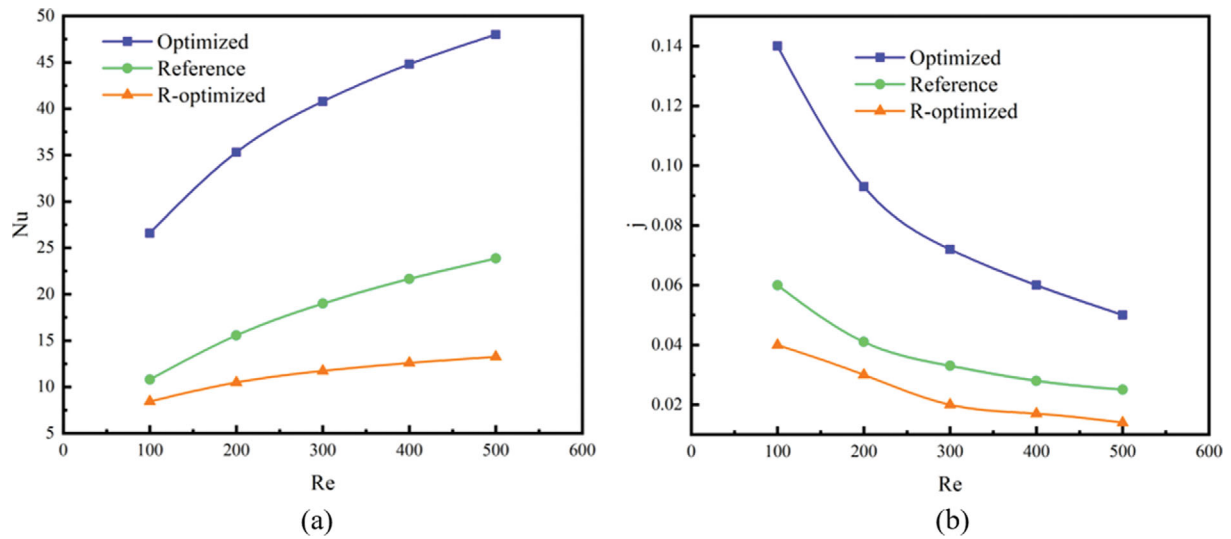The variation of the maximum surface temperature is particu-

Fig. 8. (a)The variation of j under different Res (b)The variation of Nu under different Res.

Table 7. Basal average temperature and pressure drop values at different Res

Re	100	200	300	400	500
Average temperature	321.20 K	312.66 K	309.69 K	308.15 K	307.19 K
Pressure drops	31,762 Pa	89,577 Pa	177,570 Pa	297,600 Pa	448,530 Pa

larly important when studying heat exchangers used to dissipate heat from electronic chips, but the average temperature of the chip surface is also an important indicator of good heat transfer performance. Table 7 shows the values of the optimized average substrate temperature and pressure drop with different Res.

For Re=100, the average temperature of the substrate is 321.20 K, and the pressure drop is 31,762 Pa. For Re=500, the average temperature of the substrate is 307.19 K, and the pressure drop is 448,530 Pa. The temperature decreases by 14.01 K or 4.39%. The pressure drop increased by nearly 14 times.

Fig. 9 shows the changes of temperature and pressure drop in the fractal baffles microchannel at different inlet velocities. The
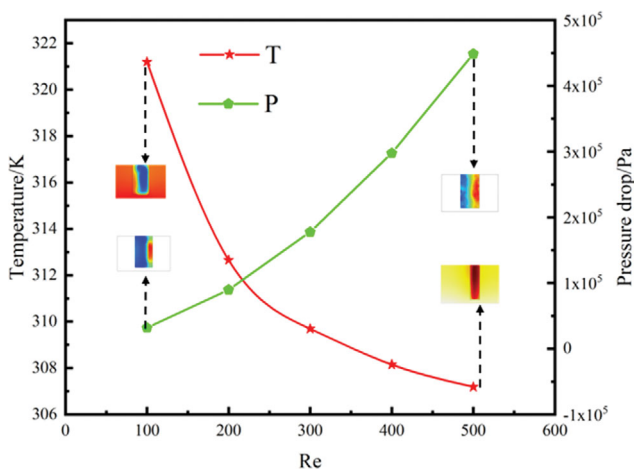
average temperature at the base of the microchannel gradually decreases and the pressure drop gradually increases as the Re increases. At low Re, the basal temperature decreases relatively fast, but with the increase of Re, the basal temperature decreases slowly. This is also consistent with the basic law of heat transfer in microchannels.

4. Comprehensive Performance Analysis

To better compare the heat transfer performance of the microchannel before and after optimization, it is more reasonable to use the enhanced heat transfer factor PEC to evaluate the comprehensive heat transfer performance of the microchannel than the entropy yield and heat transfer coefficient, and the variation of the micro-
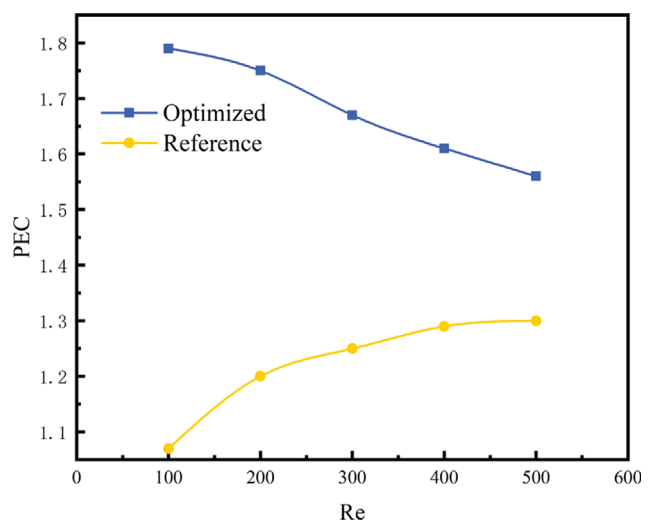

Fig. 9. Schematic diagram of the average temperature and pressure drop at different Res.

Fig. 10. Comprehensive heat transfer performance at different Res.

channel PEC factor with Re is obtained according to the previous equation.

In Fig. 10, the enhanced heat transfer factor PEC of both optimized and reference microchannels is greater than 1. In this paper, when the PEC value is greater than 1, it means that the enhanced microchannel has higher surface heat transfer coefficient than the conventional microchannel with the same pump power consumption. The higher the PEC value, the more significant the improvement in heat transfer performance, and the flattening of the PEC value indicates the high thermal stability of the heat exchanger. This indicates that the heat transfer performance of the reference microchannel is improved compared to a conventional microchannel, while the heat transfer performance of the optimized microchannel is significantly improved. The enhanced heat transfer factor PEC of the optimized microchannel structure gradually increases with the increase of Re, and its enhanced heat transfer factor PEC is 1.56-1.79 in the range of Re from 100 to 500.

CONCLUSION

We designed a novel microchannel structure by combining the cantor fractal principle with the microchannel heat sink. We chose the microchannel entrance aspect ratio (a/b), the Cantor fractal baffle aspect ratio (B/h), and the ratio of the microchannel entrance width to the distance between groups (a/λ) as design variables. The structure of the microchannel was optimized. Conclusions are as follows:

1. The maximum temperature at the bottom of the optimized microchannel is 27 °C lower than that of the conventional channel, and the Nu is increased by 2.5 times. This shows that the heat transfer of the optimized cantor fractal microchannel heat sink has been greatly improved.

2. The enhanced heat transfer factor PEC in the optimized microchannel structure gradually increases with the increase of Re. The enhanced heat transfer factor PEC is 1.56-1.79 in the range of Re from 100 to 500, indicating that the optimized microchannel heat transfer effect ratio traditional microchannels have been greatly improved.

3. By applying the fractal principle to the microchannel structure, the influence of the contact area on the cooling effect of the microchannel is verified, and the idea that increasing the contact area can improve the performance of the microchannel heat sink is proposed.

Here are some suggestions for future work:

1. A new structure is proposed for the microchannel heat sink to improve the heat transfer performance from the structure, not limited to the optimization of the structure size. Continue to improve the algorithm or seek to introduce new algorithms to get the global optimal value faster and more efficiently.

2. Carry out microchannel experimental research to provide strong support for theoretical research. Combined with theoretical research results, more effective feedback guides practical application.

ACKNOWLEDGEMENT

DATA AVAILABILITY STATEMENT

The data that support the findings of this study are available on request from the corresponding author, [Wang H]. The data are not publicly available due to [restrictions e.g. their containing information that could compromise the privacy of research participants].

DECLARATION OF CONFLICT OF INTEREST STATEMENT

The authors declare that they have no known competing financial interests or personal relationships that could have appeared to influence the work reported in this paper.

REFERENCES

1. M. Gholinia, K. Hosseinzadeh, H. Mehrzadi, D. D. Ganji and A. A. Ranjbar, *Case. Stud. Therm. Eng.*, **13**, 100356 (2019).
2. A. H. Ghobadi and M. G. Hassankolaei, *Heat. Transf. Asian. Res.*, **48**, 4262 (2019).
3. M. Gholinia, S. K. Moosavi, M. Pourfallah, S. Gholinia and D. D. Ganji, *Int. J. Amb. Energy*, **42**, 1815 (2021).
4. M. Rahimi-Gorji, L. Van de Sande, C. Debbaut, G. Ghorbaniasl, H. Braet, S. Cosyns and W. Ceelen, *Adv. Drug. Deliver. Rev.*, **160**, 105 (2020).
5. E. Anastasiou, K. O. Lorentz, G. J. Stein and P. D. Mitchell, *Lancet. Infect. Dis.*, **14**, 553 (2014).
6. M. Gholinia, K. Hosseinzadeh and D. D. Ganji, *Case. Stud. Therm. Eng.*, **21**, 100666 (2020).
7. M. Gholinia, A. A. Ranjbar, M. Javidan and A. A. Hosseinpour, *Energy Rep.*, **7**, 6844 (2021).
8. A. Dewan and P. Srivastava, *J. Therm. Sci.*, **24**, 203 (2015).
9. M. M. Sarafraz, V. Nikkhah, M. Nakhjavani and A. Arya, *Exp. Therm. Fluid. Sci.*, **91**, 509 (2018).
10. S. V. Garimella and V. Singhal, *Heat. Transfer. Eng.*, **25**, 15 (2004).
11. H. A. Mohammed, P. Gunnasegaran and N. H. Shuaib, *Int. Commun. Heat. Mass. Transf.*, **38**, 474 (2011).
12. M. Gholinia, S. A. H. Kiaeian Moosavi, S. Gholinia and D. D. Ganji, *Heat. Transf. Asian. Res.*, **48**, 3278 (2019).
13. A. H. Ghobadi, M. Armin, S. G. Hassankolaei and M. Gholinia Hassankolaei, *Int. J. Amb. Energy*, **41**, 1 (2020).
14. M. Gholinia, M. Armin, A. A. Ranjbar and D. D. Ganji, *Case. Stud. Therm. Eng.*, **14**, 100490 (2019).
15. S. S. Ghadikolaei, M. Gholinia, M. E. Hoseini and D. D. Ganji, *J. Taiwan. Inst. Chem. E.*, **97**, 12 (2019).
16. A. A. Yagodnitsyna, A. V. Kovalev and A. V. Bilsky, *J. Phys. Confer.*, **899**, 032026 (2017).
17. P. Kumar, *Int. J. Therm. Sci.*, **136**, 33 (2019).
18. M. Xu, H. Lu, L. Gong, J. C. Chai and X. Duan, *Int. Commun. Heat. Mass. Transf.*, **76**, 348 (2016).
19. Y. Sui, C. J. Teo, P. S. Lee, Y. T. Chew and C. Shu, *Int. Commun. Heat. Mass. Transf.*, **53**, 2760 (2010).
20. H. A. Mohammed, P. Gunnasegaran and N. H. Shuaib, *Int. Com-*

mun. Heat. Mass. Transf., **38**, 63 (2011).

21. L. Chai, G. Xia, L. Wang, M. Zhou and Z. Cui, *Int. J. Heat. Mass. Transf.*, **62**, 741 (2013).

22. G. Xia, L. Chai, M. Zhou and H. Wang, *Int. J. Therm. Sci.*, **50**, 411 (2011).

23. L. Chai, G. D. Xia and H. S. Wang, *Int. J. Heat. Mass. Transf.*, **97**, 1069 (2016).

24. L. Chai, G. D. Xia and H. S. Wang, *Int. J. Heat. Mass. Transf.*, **97**, 1091 (2016).

25. H. Garg, V. S. Negi, A. S. Wadhwa and A. K. Lall, *RAECS*, 1 (2014).

26. G. Wang, T. Chen, M. Tian and G. Ding, *Int. J. Heat. Mass. Transf.*, **148**, 119142 (2020).

27. I. A. Ghani, N. A. C. Sidik, R. Mamat, G. Najafi, T. L. Ken, Y. Asako and W. M. A. A. Japar, *Int. J. Heat. Mass. Transf.*, **114**, 640 (2017).

28. L. Chai, G. Xia, M. Zhou, J. Li and J. Qi, *Appl. Therm. Eng.*, **51**, 880 (2013).

29. Z. Shi and T. Dong, *Energy Convers. Manage.*, **94**, 493 (2015).

30. J. Zhang, Y. Zhao, Y. Diao and Y. Zhang, *Int. J. Heat. Mass. Transf.*, **84**, 511 (2015).

31. T. Ambreen and M. H. Kim, *Int. J. Heat. Mass. Transf.*, **120**, 490 (2017).

32. E. Manay, E. F. Akyürek and B. Sahin, *Results. Phys.*, **9**, 615 (2018).

33. K. Hosseinzadeh, M. Gholinia, B. Jafari, A. Ghanbarpour, H. Olfian and D. D. Ganji, *Heat. Transf. Asian. Res.*, **48**, 744 (2019).

34. A. H. Ghobadi and M. G. Hassankolaei, *Heat. Transf. Asian. Res.*, **48**, 4133 (2019).

35. K. Hosseinzadeh, F. Afsharpanah, S. Zamani, M. Gholinia and D. D. Ganji, *Case. Stud. Therm. Eng.*, **12**, 228 (2018).

36. O. Khandouzi, M. Pourfallah, E. Yoosefirad, B. Shaker, M. Gholinia and S. Mouloodi, *J. Energy Storage.*, **37**, 102464 (2021).

37. S. Shahlaei and M. G. Hassankolaei, *Heat. Transf. Asian. Res.*, **48**, 4152 (2019).

38. J. Li and G. P. Peterson, *Int. J. Heat. Mass. Transf.*, **50**, 2895 (2007).

39. Y. Chen, P. Fu, C. Zhang and M. Shi, *Int. J. Heat. Fluid. Flow.*, **31**, 622 (2010).

40. N. Mohd-Ghazali, O. Jong-Taek, N. B. Chien, C. Kwang-Il, N. A. Zolpakar and R. Ahmad, *Energy Procedia*, **61**, 55 (2014).

41. A. M. Adham, N. Mohd-Ghazali and R. Ahmad, *Arab. J. Sci. Eng.*, **39**, 7211 (2014).

42. H. Lv, X. Chen and X. Zeng, *Chaos. Soliton. Fract.*, **148**, 111048 (2021).

43. K. X. Cheng, Z. H. Foo and K. T. Ooi, *Int. Commun. Heat. Mass. Transf.*, **111**, 104456 (2020).

44. J. Y. Yun and K. S. Lee, *Int. J. Heat. Mass. Transf.*, **43**, 2529 (2000).

45. Y. Liu, J. Cui, W. Li and N. Zhang, *J. Heat. Transf.*, **133**, 12 (2011).

46. Y. Alperen and C. Sertac, *Int. J. Heat. Mass. Transf.*, **146**, 118847 (2020).